




Phononic Doppler effect in sliding friction

Yi Tao ¹, Yun Dong^{1,2}, Yajing Kan¹, Zhiyong Wei¹, Yan Zhang¹, Chenhan Liu ^{3,*} and Yunfei Chen ^{1,†}

¹*Jiangsu Key Laboratory for Design and Manufacture of Micro-Nano Biomedical Instruments,*

School of Mechanical Engineering, Southeast University, Nanjing 211189, China

²*School of Mechanical and Electrical Engineering, Lanzhou University of Technology, Lanzhou 730050, China*

³*School of Energy and Mechanical Engineering, Nanjing Normal University, Nanjing, 210023, China*



(Received 28 November 2023; revised 11 April 2024; accepted 22 April 2024; published 7 May 2024)

The Doppler effect plays a fundamental role in a vast array of applications, spanning from the quantum domain to cosmic scales. Nevertheless, its manifestation in the context of phonon excitation during the friction between two objects with relative motion remains unexplored. In this study, we predict and investigate the occurrence of the phononic Doppler effect within sliding friction, employing a phononic dynamics model derived through the atomistic Green's function method. As the friction-excited phonons propagate both forward and backward relative to the moving object, we predict frequency high-shift and low-shift phenomena, respectively. We propose a phonon excitation rule, grounded in the phonon dispersion relation, to elucidate the frequency-shift behavior, essentially capturing the Doppler effect on friction-excited phonons. The predicted frequency shift, as determined by the phonon excitation rule, finds validation through molecular dynamics simulations. The observation of the phononic Doppler effect in sliding friction opens a range of potential applications, providing innovative tools for detecting energy-dissipation mechanisms at interfaces caused by friction.

DOI: [10.1103/PhysRevB.109.205410](https://doi.org/10.1103/PhysRevB.109.205410)

I. INTRODUCTION

The Doppler effect is a well-established phenomenon that results in a shift in the frequency of waves emitted from an object in motion, relative to the frequency at the source [1]. This effect has diverse applications, from speed measurements in vehicles and blood-flow monitoring to aircraft radar systems and global positioning systems via satellite [2–5]. In addition to its numerous successful applications on a macroscopic scale, the Doppler effect also holds significant relevance at the quantum level. For instance, the Doppler effect can facilitate the cooling and trapping of atoms through photon interactions [6,7]. Much like the acoustic waves emitted from a moving source, friction-excited lattice waves are results of the relative motion between two objects in contact. Given this, it is reasonable to assume that the Doppler effect would also manifest in these friction-excited lattice waves, i.e., phonons.

Friction, which arises from the relative motion between two objects in contact, has been extensively studied over the centuries. Numerous phenomenological models, such as the Prandtl-Tomlinson model and various rate-and-state friction models [8–11], have been developed to shed light on the mechanisms of friction across a broad range of scales, e.g., from nanoscopic interactions observed in atomic force microscope [12,13] to macroscopic phenomena like earthquakes [14]. However, these models have limitations, particularly in their neglect of energy-dissipation mechanisms like waves or quantized phonon excitations. As a result, they fall short in

their ability to predict unknown physical phenomena. In this study, we present predictions of the Doppler effect in friction-excited phonons using our proposed phononic dynamics (PD) model, which is derived from the atomistic Green's function method. The model indicates the high shifts and low shifts of frequency in phonons excited at the front and rear of the moving object, respectively. Also, a phonon excitation rule is proposed to capture the frequency-shift properties of friction-excited phonons based on the phonon dispersion relation. These predictions are further corroborated by molecular dynamics (MD) simulations.

II. PREDICTED FRICTION FORCE BY PHONONIC DYNAMICS MODEL

In our previous work, a preliminary PD model to study the friction-excited phonon dynamics was proposed, which could explore the phonon excitations in sliding friction with infinite contacted size along sliding direction [15]. To investigate the Doppler effect, it is essential to constrain the contact size to a finite dimension along the sliding direction, i.e., the x -axis direction, while a periodic boundary condition is applied solely along the y -axis direction. As illustrated in Fig. 1(a), the friction system simulates the sliding of a finite-sized graphene flake over another graphene substrate in the zigzag direction. The width of the substrate is the same as that of the flake, but its length along the sliding direction is significantly greater. We can define five distinct regions in the friction system according to the slider position. These include the virtual support region (VSR), which drags the upper flake to slide forward; the slider region (SR), corresponding to the upper graphene flake with each atom connecting with the virtual

*Corresponding author: chenhanliu@njnu.edu.cn

†Corresponding author: yunfeichen@seu.edu.cn

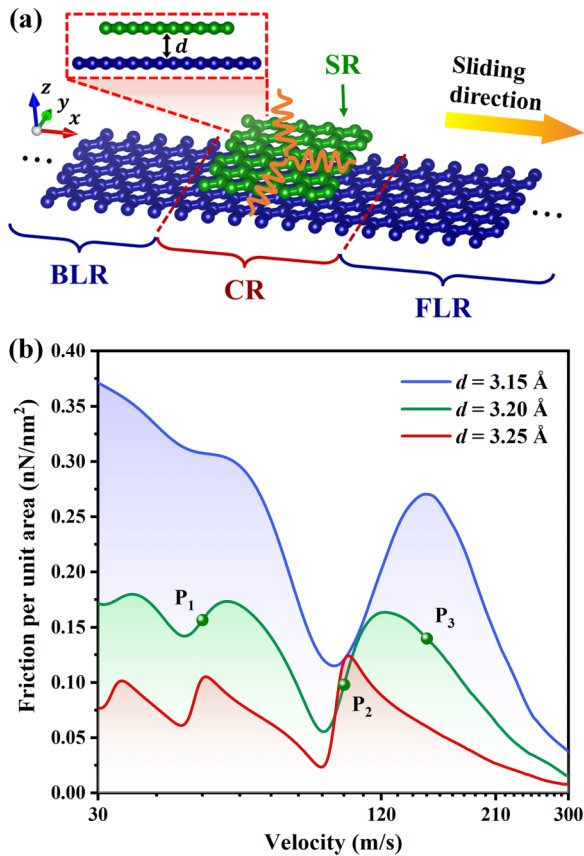


FIG. 1. (a) Schematic illustration of the friction system contains a graphene flake sliding over another graphene substrate. The variable d represents the interfacial distance between the slider and the substrate. (b) Predicted friction forces per unit area by the PD model under three different interfacial distances.

support through three springs along the x -, y -, and z -axis directions; the contact region (CR), representing the region where the two graphene flakes come into contact; the semi-infinite forward-lead region (FLR), designating the substrate area in front of the upper graphene flake along the sliding direction; and the semi-infinite backward-lead region (BLR) in the substrate, located behind the upper graphene flake as shown in Fig. 1(a). The sliding graphene flake subsequently triggers atomic vibrations in CR, with the phonons excited at both the front and back of the graphene slider. Then, the excited phonons propagate into the semi-infinite FLR and BLR, inducing the dissipation of systemic energy and thus the friction. Notice that in this friction system, the contact area, which possesses a finite size, progresses concurrently with the moving slider. This is in contrast to the stationary infinite contact area applied in our prior PD model [15]. The movement of the contact area amplifies the complexity of solving for phonon excitation and propagation. Consequently, we have developed a more universal algorithm to address the challenges presented by such a realistic friction system. (see Appendix A for detailed derivations).

To get the solutions of the PD model for the friction system in Fig. 1(a), the intralayer C-C interactions of graphene are simulated by the Tersoff potential [16], while the interlayer C-C interactions are simulated by the Lennard-Jones

potential [17], respectively. All the springs have a uniform stiffness at 0.1 N/m. Figure 1(b) illustrates the variation of the friction force, in relation to the interfacial distance d between the slider and substrate. The calculated friction force demonstrates the similar nonmonotonic velocity dependence as observed in our recent experiments [18]. Multiple friction peaks occur within the sliding velocity range of 30 to 300 m/s. These peaks are attributed to the resonant vibration of the friction system induced by excited phonons [18]. In addition, as the interfacial distance decreases, the normal load increases, leading to an enhancement in the friction force and a shift of the friction peak to a higher sliding velocity.

III. NUMBER DENSITY OF FRICTION-EXCITED PHONONS

It is reported that the phonons excited by friction are usually peaked at washboard frequency ($f_0 = v_0/a_x$) and its harmonics [15,18], where v_0 is the sliding velocity and a_x is the lattice constant of the substrate along the sliding direction. To explore the characteristics of friction-excited phonons in the friction system with finite contact area, the number density of excited phonons in FLR and BLR is calculated with different sliding velocities for $d = 3.20 \text{ \AA}$ as shown in Fig. 2. Contrasting with our previous findings, where friction-excited phonons were distributed discretely at nf_0 (n is a integer) [15,18], the current observations indicate that phonons excited in the BLR shift to lower frequencies than nf_0 , exhibiting a low shift. Conversely, phonons excited in the FLR shift to higher frequencies, indicative of a high shift. This behavior aligns precisely with the Doppler effect [1]. Besides, the observed singular peak of the phonon number density at nf_0 [18] splits into several distinct peaks. The frequency shift becomes larger for the phonons with higher excitation frequency or for higher sliding velocity as shown in Fig. 2.

To interpret the phonon frequency shift, Fig. 3(a) provides a schematic representation of the phononic Doppler effect as it relates to sliding friction. As the graphene flake moves across the graphene substrate, it compresses the excited waves in the FLR. This compression pushes the waves to move forward relative to the sliding graphene, which subsequently shortens their wavelength and raises the excitation frequency. On the other hand, in the BLR, the moving source consistently stretches the excited waves, resulting in a lengthened wavelength and a decreased excitation frequency. Based on the theory of phonon propagation, a rule governing the frequency shift of phonon excitation can be established as depicted in Fig. 3(b) (see Appendix B for detailed derivations). In Fig. 3(b), two distinct lines intersect the dispersion curves: the static line, represented by the magenta dashed line, and the kinematic line, represented by the slanting orange solid line with the slope of $v_0/2\pi$. As depicted in Fig. 3(a), the phonons excited in FLR have positive wave vector and their dynamics is governed by the phonon dispersion relation in the right panel of Fig. 3(b), while in the left panel of Fig. 3(b), the phonon dispersion relation with negative wave vector governs the dynamics of phonons excited in BLR. If the Doppler effect were neglected, the frictional phonons would be excited at f_0 and its harmonics in both FLR and BLR [15]. The properties of those phonons could be predicted by the

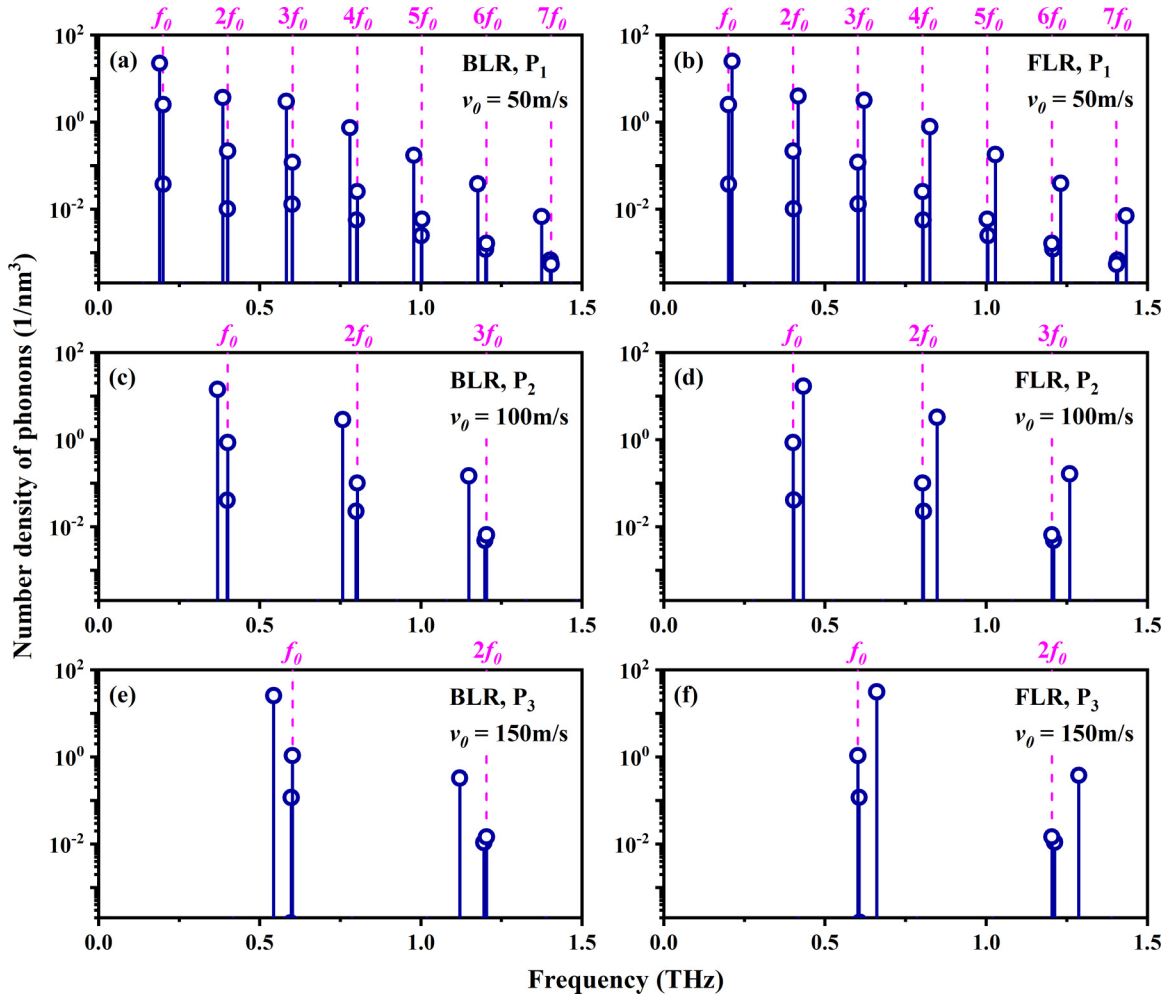


FIG. 2. The number density of excited phonons at different sliding velocities for $d = 3.20 \text{ \AA}$. The labels from P_1 to P_3 in the legends correspond to the marked points in Fig. 1(b), while the dashed magenta lines denote the washboard frequency (f_0) and its harmonics.

intersections between the static lines and phonon dispersion relation curves, including longitudinal acoustic (LA) mode, transverse acoustic (TA) mode, and flexural acoustic (ZA) mode. Considering the Doppler effect, as depicted in Fig. 3(b), the characteristics of friction-excited phonons are determined by the points where the kinematic lines intersect the dispersion relation curves. Consequently, the friction-excited phonons in FLR manifest higher frequencies, while the excited phonons in BLR display lower frequencies. Additionally, the Doppler effect imparts varying contributions to the frequency shifts of friction-excited LA, TA, and ZA modes. This is why the number density of the excited phonons demonstrates three distinct peaks near nf_0 , as presented in Fig. 2.

Intriguingly, as the frequency increases, the points where kinematic lines intersect with dispersion curves diverge further from those where static lines intersect with dispersion curves as depicted in Fig. 3(b). This suggests that phonons excited by higher harmonics experience a more significant frequency shift. When the sliding velocity is increased, the frequency shift becomes even more pronounced, since the slope of the kinematic line is directly proportional to the sliding velocity. Consequently, the phonon excitation pattern demonstrated in Fig. 3(b) aptly elucidates the pronounced

frequency shifts seen in Fig. 2, both for higher phonon excitation frequencies and increased sliding velocities.

IV. DOMINATED PHONON MODE IN ENERGY DISSIPATIONS

Given a specific sliding velocity, the phonons excited in the ZA mode exhibit the highest frequency shift. This is because these phonons possess larger wave vectors compared to those in the LA or TA modes as illustrated in Fig. 3(b), which can be attributed to the parabolic property of ZA mode. In Fig. 2, three distinct peaks are evident near each nf_0 , corresponding to the ZA, TA, and LA phonon modes, respectively. From the observed frequency shift, it is evident that the highest peak amplitude should be attributed to the ZA mode, as it displays the most significant frequency shift among the three components. The observed peak amplitude prominence for the ZA mode suggests an unexpectedly high excitation number of these phonons during the friction process, contrary to conventional expectations. Typically, one might predict that atomic lateral vibrations would be more easily excited by friction as the slider moves in the plane of graphene [15], leading to a presumption that energy dissipation would be primarily via

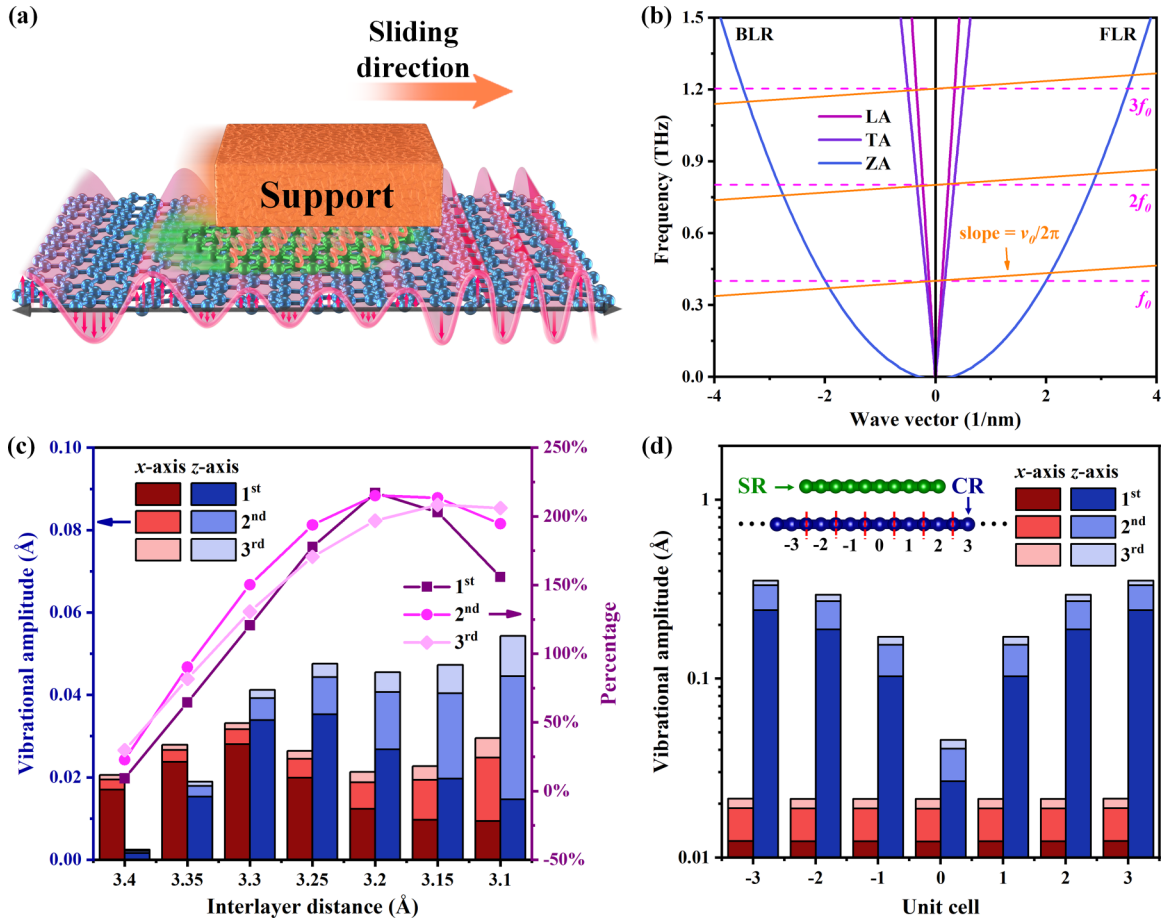


FIG. 3. (a) Schematic diagram of the phononic Doppler effect in sliding friction. (b) Phonon dispersion relation of the graphene substrate. (c) The vibrational amplitudes of the n th harmonic for atoms positioned at the center unit cell of the CR, along the x - and z axes. The right vertical axis represents the ratio of the vibrational amplitude along the z axis to that along the x axis. (d) The vibrational amplitudes of the n th harmonic along the x - and z -axis directions for atoms located within various unit cells in the CR, with the inset denoting the position of each unit cell. The sliding velocity is $v_0 = 100\text{m/s}$ for (b), (c), and (d), and $d = 3.20\text{Å}$ for (d).

LA mode phonons. The counterintuitive observation can be explained by the properties of friction-induced vibrations for atoms within the central unit cell of the CR, as depicted in Fig. 3(c). At a considerable interfacial distance of $d \geq 3.35\text{Å}$, which equates to a lesser normal load, atomic vibrational amplitude along the x axis is greater than those along the z axis. Yet, as the interfacial distance diminishes to 3.3Å or less, vibrational amplitude along the z axis exceeds that along the x axis. It is because as the slider traverses the substrate, atoms within the CR are subjected to the perturbative forces from the slider atoms. These forces follow a vector path extending directly from the slider atoms to those within the CR. Since the slider atoms are homogeneously distributed over the CR atoms, their x -axis components of the perturbative forces imparted to the CR atom partially neutralize each other, and exhibit minimal dependence on the normal load. However, their z -axis components of the perturbative forces on the CR atom are consistently aligned with the normal-load axis, leading to an increase in the z -axis vibrational amplitude as the interfacial distance narrows from 3.4 to 3.25Å . In addition, observations indicate that within the central unit cell of CR, the first-order vibrational amplitude along the z axis, and its ratio to that along the x axis, are repressed for $d < 3.25\text{Å}$.

For the high-order harmonic vibrations, their amplitudes start to decrease at a smaller interfacial distance. The observations suggest that higher normal load may also suppresses atomic vibrations along the z axis within CR. Although the z -axis atomic vibrations in central CR atoms are suppressed by high normal load for $d = 3.20\text{Å}$, the peripheral CR atoms are less affected by the normal load. This results in pronounced z -axis movements for these peripheral atoms as shown in Fig. 3(d). It should be noticed that the phonon modes excited in FLR and BLR are largely determined by the vibrational properties of peripheral CR atoms situated adjacent to these regions. Therefore, the prominent z -axis movements of peripheral CR atoms facilitate the abundant excitation of ZA mode phonons in FLR and BLR.

V. VALIDATION OF MOLECULAR DYNAMICS SIMULATIONS

To verify the predicted frequency shifts from the PD model, MD simulations are performed with the model presented in Fig. 4(a). The spring stiffness and atomic interactions are set the same as those in the PD model, while the sliding velocity and normal load are set at 100m/s and

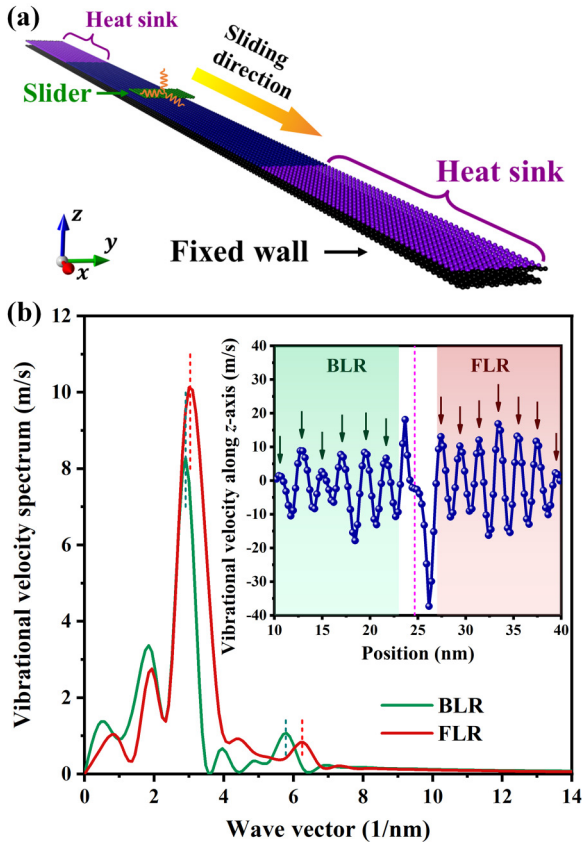


FIG. 4. (a) Schematic illustration of a MD model to simulate a slider moving across a substrate with a constant velocity. (b) The calculated vibrational velocity spectrum vs wave vector, which is the SFFT of the instantaneous atomic velocity vs the atomic positions as shown in the inset. The magenta dashed line in the inset denotes the central position of the slider.

0.1 nN per atom, respectively (see Appendix C for details). The inset in Fig. 4(b) illustrates the vibrational velocities of substrate atoms along the z axis at a specified instant. The predominance of the z -axis vibrational component of the excited waves indicates a substantial contribution of the ZA phonon mode to the energy dissipation in friction. This observation is in alignment with the predictions made by the PD model. During the sliding process, the substrate atoms at the leading edge of the slider tend to move downward in response to the normal load. This movement results in the formation of a discernible “negative velocity valley” in close proximity to the front of the slider, as depicted in the inset of Fig. 4(b). In contrast, the remarkable “positive velocity peak” at the trailing edge of the slider results from the rebound of substrate atoms as the slider advances over them. Notably, more velocity peaks are present in the FLR than in the BLR over the same distance, marked by arrows in the inset of Fig. 4(b), indicating a more densely excited wave in the FLR than that in the BLR. To substantiate this observation, we performed a spatial fast Fourier transform (SFFT) of the atomic vibrational velocities along the z axis, a method routinely used to identify the wave vectors of excitation waves.

As depicted in Fig. 4(b), the atomic vibrational velocity spectrum reaches its highest peaks at wave vectors of

$\kappa_F = 3.16 \text{ nm}^{-1}$ in FLR and $\kappa_B = 2.87 \text{ nm}^{-1}$ in BLR, respectively. These wave vectors correspond to average wavelengths estimated by the relationship $\lambda_{F/B} = 2\pi/\kappa_{F/B}$. Consequently, the average wavelength in the FLR can be estimated as $\lambda_F \sim 1.99 \text{ nm}$, whereas in the BLR, it is approximately $\lambda_B \sim 2.19 \text{ nm}$. These measurements confirm that elastic waves are compressed in the FLR and elongated in the BLR, demonstrating a classic Doppler effect. For the second-order harmonic vibration at $\sim 6 \text{ nm}^{-1}$, there is a greater disparity in the wave vectors of phonons excited in FLR compared to those in the BLR. These empirical findings are in excellent concordance with the theoretical predictions presented in Fig. 3(b), which indicate that the Doppler effect has a significant impact on the wave-vector differences of friction-excited phonons, especially for the ZA-mode phonons. Besides, the influence of the Doppler effect is more pronounced in higher-order harmonic excitations.

VI. CONCLUSION

In summary, our developed phononic dynamics model reveals the presence of the phononic Doppler effect in sliding friction. We observe clear high shift and low shift of frequency in friction-excited phonons as they propagate forward and backward relative to the moving object, respectively. The Doppler effect manifests varying contributions to the frequency shift in the LA, TA, and ZA modes, resulting in a frequency split among the excited phonons. To precisely predict the frequency shift for different phonon modes due to the Doppler effect, we establish a phonon excitation rule based on phonon dispersion relations. The established rule is pivotal for unraveling the complex processes of energy dissipation during sliding friction. For instance, by examining the frequency shifts in LA, TA, and ZA modes, we have identified that ZA-mode phonons play the most significant role in the dissipation of energy due to friction in layered materials. This insight has been corroborated by MD simulations. Given the broad range of applications of the Doppler effect, the discovery of its presence in sliding friction opens up innovative possibilities for friction detection.

ACKNOWLEDGMENTS

The authors acknowledge the financial support from the Natural Science Foundation of China (Grants No. 52035003, No. 52127811, No. 52175161, and No. 52206092), the Natural Science Foundation of Jiangsu Province (Grant No. BK20210565), the China Postdoctoral Science Foundation (Grant No. 2022M710676), the Excellent Postdoctoral Project of Jiangsu Province (Grant No. 2022ZB104), the Department of Science and Technology of Jiangsu Province (Grants No. BK20230843, No. BK20222005, and No. BK20220032). C.L. was funded by the Basic Science (Natural Science) Research Project of Higher Education Institutions of Jiangsu Province (Grant No. 21KJB470009), Nanjing Science and Technology Innovation Project for Overseas Students, “Shuangchuang” Doctor program of Jiangsu Province (Grant No. JSSCBS20210315), and open research fund of Jiangsu Key Laboratory for Design and Manufacture of Micro-Nano Biomedical Instruments, Southeast University (Grant No.

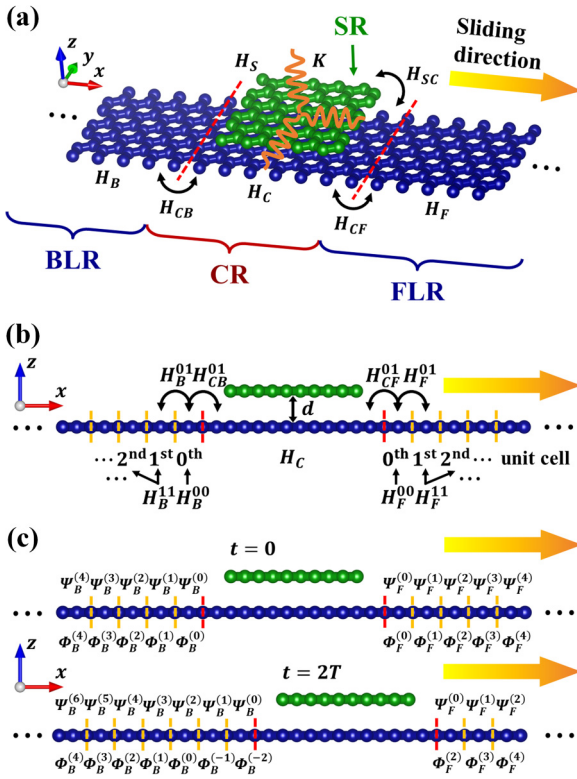


FIG. 5. (a) Schematic diagram of a graphene flake sliding over another graphene substrate. (b) The side view of the friction system with meshed unit cells in FLR and BLR, respectively. (c) The side view of the friction system at the time moments $t = 0$ and $t = 2T$ for examples.

KF202010). The authors acknowledge the Big Data Center of Southeast University for performing the numerical calculations presented in this paper.

APPENDIX A: DETAILED DERIVATIONS OF EXTENDED PHONONIC DYNAMICS MODEL

The PD model is set up with the atomistic Green's function method, in which the atomic interactions are approximated with the harmonic interactions. As shown in Fig. 5(a), the friction system simulates a finite-sized graphene flake sliding over another graphene substrate in the zigzag direction. The width of the substrate is the same as that of the flake, but its length along the sliding direction is significantly greater. We can define five distinct regions in the friction system according to the slider position. These include the VSR, the SR, the CR, the semi-infinite FLR, and the semi-infinite BLR, as shown in Fig. 5(a).

Ignoring the anharmonic terms, the second-order force constants calculated from LAMMPS [19] are used to build the harmonic matrix H , where the intralayer and interlayer interactions of graphene are modeled by Tersoff potential [16] and Lennard-Jones potential [17], respectively:

$$H = \{H_{i\alpha j\beta}\} = \frac{1}{\sqrt{M_i M_j}} \begin{cases} \frac{\partial^2 E}{\partial u_{i\alpha} \partial u_{j\beta}}, & \text{if } i \neq j \\ -\sum_{r \neq j} \frac{\partial^2 E}{\partial u_{r\alpha} \partial u_{j\beta}}, & \text{if } i = j \end{cases}, \quad (\text{A1})$$

where M_i and $u_{i\alpha}$ refer to atomic mass for each atom i and corresponding atomic displacement for atom i along α - (x -, y -, or z -) direction, and E represents the interatomic potential energy related to atomic displacements.

If the driving spring stiffness is set high enough, the slider will conduct only single slip. Thus, the motion equation for slider atoms can be derived as [15]

$$\ddot{\Phi}_S(t) = -K(\Phi_V(t) - \Phi_S(t)) - H_S(\Phi_S(t) - a_S) - H_{SC}\Psi_C(t), \quad (\text{A2})$$

where the subscripts V , S , C , F , and B represent VSR, SR, CR, FLR, and BLR, respectively. H_I is the harmonic matrix corresponding to region I , while H_{IJ} is the harmonic matrix corresponding to the coupling between region I and region J . $\Phi_S(t)$ represents the matrix of atomic displacements multiplied by the square root of the corresponding atomic mass (SRM) in SR, while $\Psi_{C/F/B}(t)$ represents that in CR, FLR, or BLR. For CR, FLR, and BLR, a different symbol $\Psi(t)$ is used to represent the atomic displacements multiplied by SRM, because these regions move with the slider. When the slider moves a distance of a_x in the sliding direction after a complete slip-stick period at the time moment $(w + 1/2)T$, CR, FLR, and BLR advance by the same distance, while the atoms in these regions are updated with the new ones according to the new positions of advanced regions. a_x represents the lattice constant of the substrate along the x -axis direction, i.e., the zigzag direction of graphene in this work, and w is an integer. $T = v_0/a_x$ is the slip-stick period, and v_0 represents the average sliding velocity of slider, which is also the same as the driving velocity of the support. $\Phi_V(t)$ and a_S represent the matrix of support displacement multiplied by the SMR and the matrix of lattice dot, which can be expressed as

$$\Phi_V(t) = \begin{bmatrix} (v_0 t + r)\sqrt{M_1} \\ 0 \\ 0 \\ (v_0 t + r)\sqrt{M_2} \\ 0 \\ 0 \\ \vdots \end{bmatrix}, \quad a_S = \begin{bmatrix} ha_x\sqrt{M_1} \\ 0 \\ 0 \\ ha_x\sqrt{M_2} \\ 0 \\ 0 \\ \vdots \end{bmatrix}, \quad (\text{A3})$$

where M_i in Eq. (A3) represents the atomic mass of corresponding slider atom connecting to the support by springs, and h is an integer to ensure $-a_x/2 \leq u_{S,ix} - ha_x < a_x/2$. r represents the average relative displacement between the support and slider; $v_0 t$ can be treated as the average slider displacement; and K is a diagonal spring stiffness harmonic matrix as defined in our preliminary PD model [15].

To simplify the motion equation, we set $\Phi_S^*(t) = \Phi_S(t) - \Phi_V(t)$, $\Phi_V^*(t) = \Phi_V(t) - a_S$, and $H_S^* = H_S - K$, and Eq. (A2) can be rewritten as

$$\ddot{\Phi}_S^*(t) = -H_S^*\Phi_S^*(t) - H_S^*\Phi_S^*(t) - H_{SC}\Psi_C(t). \quad (\text{A4})$$

Equation (4) is derived considering $\ddot{\Phi}_V(t) = 0$. The motion equation for atoms in CR can be derived similar to Eq. (A4) as

$$\ddot{\Psi}_C(t) = -H_{CS}(\Phi_S(t) - a_S) - H_C\Psi_C(t) - H_{CF}\Psi_F(t) - H_{CB}\Psi_B(t). \quad (\text{A5})$$

Notice that $\Phi_S(t) - a_S = \Phi_S^*(t) + \Phi_V^*(t)$. Thus, Eq. (A5) can be rewritten as

$$\ddot{\Psi}_C(t) = -H_{CS}(\Phi_S^*(t) + \Phi_V^*(t)) - H_C\Psi_C(t) - H_{CF}\Psi_F(t) - H_{CB}\Psi_B(t). \quad (\text{A6})$$

And, the motion equations for atoms in FLR and BLR can be derived, respectively, as

$$\ddot{\Psi}_F(t) = -H_{FC}\Psi_C(t) - H_F\Psi_F(t), \quad (\text{A7})$$

$$\ddot{\Psi}_B(t) = -H_{BC}\Psi_C(t) - H_B\Psi_B(t). \quad (\text{A8})$$

Notice that $\Phi_V^*(t)$ in Eq. (A4) and Eq. (A6) can be decomposed using discrete Fourier transform as

$$\Phi_V^*(t) = \begin{bmatrix} \sqrt{M_1}(v_0t + r - ha_x) \\ 0 \\ 0 \\ \sqrt{M_2}(v_0t + r - ha_x) \\ 0 \\ 0 \\ \vdots \end{bmatrix} = \begin{bmatrix} \sum_n \frac{a_x \sqrt{M_1} (-1)^n}{n\pi} \text{Im}(e^{-in\omega t}) + r\sqrt{M_1} \\ 0 \\ 0 \\ \sum_n \frac{a_x \sqrt{M_2} (-1)^n}{n\pi} \text{Im}(e^{-in\omega t}) + r\sqrt{M_2} \\ 0 \\ 0 \\ \vdots \end{bmatrix}, \quad (\text{A9})$$

where ω is the washboard angular frequency defined as $\omega = 2\pi v_0/a_x$, and n is the positive integer varying from 1 to ∞ . To simplify the calculations, we substitute $\text{Im}(e^{-in\omega t})$ with the complex number $e^{-in\omega t}$ to account for atomic vibrations in the following calculation, which does not affect the results. Also, the constant r representing the average relative displacement between slider and support, i.e., the average extension of spring, is ignored in the following derivations, because it is the atomic vibrations that make major contributions to the phonon excitation. Thus, $\Phi_V^*(t)$ can be expanded in the Fourier series of $\sum_n \phi_{V,n}^* e^{-in\omega t}$. According to the linear response theory, $\Phi_S^*(t)$, $\Psi_C(t)$, $\Psi_F(t)$, and $\Psi_B(t)$ in Eqs. (A4)–(A8) can be expanded as the Fourier series of $\sum_n \phi_{S,n}^* e^{-in\omega t}$, $\sum_n \psi_{C,n} e^{-in\omega t}$, $\sum_n \psi_{F,n} e^{-in\omega t}$, and $\sum_n \psi_{B,n} e^{-in\omega t}$, respectively. The relations among $\phi_{V,n}^*$, $\phi_{S,n}^*$, $\psi_{C,n}$, $\psi_{F,n}$, and $\psi_{B,n}$ can be expressed in the frequency-domain matrix form as

$$\left((n^2\omega^2 + i\eta)I - \begin{bmatrix} H_S^* & H_{SC} & 0 & 0 \\ H_{CS} & H_C & H_{CF} & H_{CB} \\ 0 & H_{FC} & H_F & 0 \\ 0 & H_{BC} & 0 & H_B \end{bmatrix} \right) \begin{bmatrix} \phi_{S,n}^* \\ \psi_{C,n} \\ \psi_{F,n} \\ \psi_{B,n} \end{bmatrix} = \begin{bmatrix} H_S \phi_{V,n}^* \\ H_{CS} \phi_{V,n}^* \\ 0 \\ 0 \end{bmatrix}, \quad (\text{A10})$$

where η is a positive infinitesimal as defined in previous literature [15,20,21].

Notice that H_F , H_B , H_{CF} , H_{FC} , H_{CB} , and H_{BC} in Eq. (A10) are semi-infinite matrices defined in the semi-infinite lead regions as shown in Fig. 5(a), which makes Eq. (A10) hard to solve. To make Eq. (A10) solvable, we need to mesh FLR and BLR into unit cells, with each unit cell having a length of a_x . The unit cells in FLR are numbered sequentially as 0, 1, 2, ..., s , and so forth, as shown in Fig. 5(b). Similarly, the unit cells in BLR are also numbered sequentially as 0, 1, 2, ..., s , and so forth. When the slider moves a distance of a_x in the sliding direction after a complete slip-stick period, both FLR and BLR advance by the same distance. Consequently, the order numbers of unit cells in both FLR and BLR are reordered according to the new slider position. For example, the original s th unit cell in FLR is repositioned as the $(s-1)$ th unit cell, while the s th unit cell in BLR is repositioned as the $(s+1)$ th unit cell. According to the meshed unit cells in FLR and BLR, H_F , H_B , H_{CF} , H_{FC} , H_{CB} , and H_{BC} can be expressed in detail as

$$H_F = \begin{bmatrix} H_F^{00} & H_F^{01} & 0 & \dots \\ H_F^{10} & H_F^{11} & H_F^{01} & \dots \\ 0 & H_F^{10} & H_F^{11} & \dots \\ \vdots & \vdots & \ddots & \ddots \end{bmatrix}, \quad H_B = \begin{bmatrix} H_B^{00} & H_B^{01} & 0 & \dots \\ H_B^{10} & H_B^{11} & H_B^{01} & \dots \\ 0 & H_B^{10} & H_B^{11} & \dots \\ \vdots & \vdots & \ddots & \ddots \end{bmatrix}, \quad (\text{A11})$$

$$H_{CF} = \begin{bmatrix} H_{CF}^{01} & 0 & 0 & \dots \end{bmatrix}, \quad H_{CB} = \begin{bmatrix} H_{CB}^{01} & 0 & 0 & \dots \end{bmatrix}, \quad (\text{A12})$$

$$H_{FC} = \begin{bmatrix} H_{FC}^{10} \\ 0 \\ 0 \\ \vdots \end{bmatrix}, \quad H_{BC} = \begin{bmatrix} H_{BC}^{10} \\ 0 \\ 0 \\ \vdots \end{bmatrix}, \quad (\text{A13})$$

where H_{FC}^{10} , H_{CF}^{01} and H_{BC}^{10} , H_{CB}^{01} represent the harmonic matrices corresponding to the coupling between CR and the zeroth unit cell in FLR and BLR, respectively. $H_{F/B}^{00}$ is the harmonic matrix corresponding to the zeroth unit cell in FLR or BLR adjacent to CR. $H_{F/B}^{11}$, $H_{F/B}^{10}$, and $H_{F/B}^{01}$ are repeated for the unit cell with $s \geq 1$ in FLR or BLR, where $H_{F/B}^{11}$ represents the harmonic matrices corresponding to the s th unit cell in FLR or BLR, and $H_{F/B}^{10}$, $H_{F/B}^{01}$ represent the coupling between the s th unit cell and its adjacent unit cell in FLR or BLR. The definitions of H_{CF}^{01} , H_{CB}^{01} , $H_{F/B}^{11}$, $H_{F/B}^{10}$, and $H_{F/B}^{01}$ are presented in Fig. 5(b). Also, $\psi_{F,n}$ and $\psi_{B,n}$ can be expressed as follows:

$$\psi_{F,n} = \begin{bmatrix} \psi_{F,n}^{(0)} \\ \psi_{F,n}^{(1)} \\ \vdots \\ \psi_{F,n}^{(s)} \\ \vdots \end{bmatrix}, \quad \psi_{B,n} = \begin{bmatrix} \psi_{B,n}^{(0)} \\ \psi_{B,n}^{(1)} \\ \vdots \\ \psi_{B,n}^{(s)} \\ \vdots \end{bmatrix}, \quad (\text{A14})$$

where the superscripts (s) represent the atomic displacements multiplied by SRM in the s th unit cell of FLR or BLR. Through introducing the self-energy matrix of FLR and BLR

as $\Sigma_{F,n}^{00} = H_F^{01} \tilde{g}_{F,n} H_F^{10}$ and $\Sigma_{B,n}^{00} = H_B^{01} \tilde{g}_{B,n} H_B^{10}$, which represents the coupling between the corresponding zeroth unit cell and uncontacted semi-infinite lead regions, Eq. (A10) can be rewritten in the finite matrix form as [15,22,23]

$$\left((n^2\omega^2 + i\eta)I - \begin{bmatrix} H_S^* & H_{SC} & 0 & 0 \\ H_{CS} & H_C & H_{CF}^{01} & H_{CB}^{01} \\ 0 & H_{FC}^{10} & H_F^{00} + \Sigma_{F,n}^{00} & 0 \\ 0 & H_{BC}^{10} & 0 & H_B^{00} + \Sigma_{B,n}^{00} \end{bmatrix} \right) \begin{bmatrix} \phi_{S,n}^* \\ \psi_{C,n} \\ \psi_{F,n}^{(0)} \\ \psi_{B,n}^{(0)} \end{bmatrix} = \begin{bmatrix} H_S \phi_{V,n}^* \\ H_{CS} \phi_{V,n}^* \\ 0 \\ 0 \end{bmatrix}, \quad (\text{A15})$$

where $\tilde{g}_{F,n}$ and $\tilde{g}_{B,n}$ represent the uncontacted surface Green's function for FLR and BLR, which can be calculated directly under the iterative scheme as [22]

$$\tilde{g}_{F,n} = [(n^2\omega^2 + i\eta)I - H_F^{11} - H_F^{01} \tilde{g}_{F,n} H_F^{10}]^{-1}, \quad (\text{A16})$$

$$\tilde{g}_{B,n} = [(n^2\omega^2 + i\eta)I - H_B^{11} - H_B^{01} \tilde{g}_{B,n} H_B^{10}]^{-1}. \quad (\text{A17})$$

To solve Eq. (A15), the Green's function reflecting the dynamic response of the whole system at $n\omega$ must be obtained at first, which satisfies

$$\begin{bmatrix} G_{SS,n} & G_{SC,n} & G_{SF,n} & G_{SB,n} \\ G_{CS,n} & G_{CC,n} & G_{CF,n} & G_{CB,n} \\ G_{FS,n} & G_{FC,n} & G_{FF,n} & G_{FB,n} \\ G_{BS,n} & G_{BC,n} & G_{BF,n} & G_{BB,n} \end{bmatrix} \left((n^2\omega^2 + i\eta)I - \begin{bmatrix} H_S^* & H_{SC} & 0 & 0 \\ H_{CS} & H_C & H_{CF}^{01} & H_{CB}^{01} \\ 0 & H_{FC}^{10} & H_F^{00} + \Sigma_{F,n}^{00} & 0 \\ 0 & H_{BC}^{10} & 0 & H_B^{00} + \Sigma_{B,n}^{00} \end{bmatrix} \right) = I. \quad (\text{A18})$$

First, we need to define the surface Green's function $g_{F,n}$ for the contacted FLR and $g_{B,n}$ for the contacted BLR as

$$g_{F,n} = [(n^2\omega^2 + i\eta)I - H_F^{00} - \Sigma_{F,n}^{00}]^{-1}, \quad (\text{A19})$$

$$g_{B,n} = [(n^2\omega^2 + i\eta)I - H_B^{00} - \Sigma_{B,n}^{00}]^{-1}, \quad (\text{A20})$$

while the surface Green's function $g_{C,n}$ for CR can be defined as

$$g_{C,n} = [(n^2\omega^2 + i\eta)I - H_C - H_{CF}^{01} g_{F,n} H_{FC}^{10} - H_{CB}^{01} g_{B,n} H_{BC}^{10}]^{-1}. \quad (\text{A21})$$

Combining Eqs. (A18)–(A21), we can obtain the internal relationship of the Green's function as

$$G_{SS,n} = [(n^2\omega^2 + i\eta)I - H_S^* - H_{SC} g_{C,n} H_{CS}]^{-1}, \quad (\text{A22})$$

$$G_{CS,n} = g_{C,n} H_{CS} G_{SS,n}, \quad (\text{A23})$$

$$G_{FS,n} = g_{F,n} H_{FC}^{10} G_{CS,n}, \quad (\text{A24})$$

$$G_{BS,n} = g_{B,n} H_{BC}^{10} G_{CS,n}, \quad (\text{A25})$$

$$G_{CC,n} = G_{CS,n} H_{SC} g_{C,n} + g_{C,n}, \quad (\text{A26})$$

$$G_{FC,n} = g_{F,n} H_{FC}^{10} G_{CC,n}, \quad (\text{A27})$$

$$G_{BC,n} = g_{B,n} H_{BC}^{10} G_{CC,n}. \quad (\text{A28})$$

If both sides of Eq. (A15) are left multiplied by the Green's function of the whole system, $\psi_{F,n}^{(0)}$ and $\psi_{B,n}^{(0)}$ can be solved as

$$\psi_{F,n}^{(0)} = (G_{FS,n} H_S + G_{FC,n} H_{CS}) \phi_{V,n}^*, \quad (\text{A29})$$

$$\psi_{B,n}^{(0)} = (G_{BS,n} H_S + G_{BC,n} H_{CS}) \phi_{V,n}^*. \quad (\text{A30})$$

To derive the intrinsic atomic motions in the substrate, we also need to define two stationary regions based on the position of the slider at the time moment $t = 0$. The region located before the slider is termed the stationary forward-lead region (SFLR), while the region situated behind the slider is termed the stationary backward-lead region (SBLR). Unlike the continuously updating regions of FLR and BLR, SFLR and SBLR remain constant throughout the entire friction process. In SFLR, the unit cells are sequentially numbered as 0, 1, 2, ..., p , and so forth. Similarly, in SBLR, the unit cells are also numbered sequentially as 0, 1, 2, ..., p , and so forth. Based on the defined stationary regions, we define $\Phi_F^{(p)}(t)$ and $\Phi_B^{(p)}(t)$ to represent the matrices of atomic vibrational displacements multiplied by SRM in the p th unit cell of SFLR and SBLR, respectively. The relations between $\Phi_F^{(p)}(t)$, $\Phi_B^{(p)}(t)$ and $\Psi_F^{(s)}(t)$, $\Psi_B^{(s)}(t)$ [$\Psi_{F/B}(t)$ in the s th unit cell of FLR or BLR] can be reflected in Fig. 5(c). Now, considering time evolution of $\Phi_F^{(l)}(t)$ and $\Phi_B^{(l)}(t)$ in the l th unit cell of SFLR and SBLR, they satisfy the following relations as

$$\Phi_F^{(l)}(t) = \Phi_F^{(0)}(t - lT), \quad \text{for } t < \frac{T}{2}, \quad (\text{A31})$$

$$\Phi_B^{(l)}(t) = \Phi_B^{(0)}(t + lT), \quad \text{for } t \geq \frac{T}{2}. \quad (\text{A32})$$

Equation (A31) holds because at the time moment $t-lT$, the zeroth unit cell of SFLR has the same relative position as its l th unit cell at the time moment t with respect to the slider. Considering the periodic motion of the slider, the vibrational properties of atoms in the corresponding unit cells with the same position relative to the slider remain the same in each period. Equation (A32) also holds for the same reason. Notice that FLR and BLR have the same position as SFLR and SBLR at the time moment ranging from $-T/2$ to $T/2$. Thus, the time evolution of the atomic displacements in the l th unit cell of moving FLR and BLR as $\Psi_{F/B}^{(l)}(t) = \sum_n \psi_{F/B,n}^{(l)} e^{-in\omega t}$ must equal $\Phi_{F/B}^{(l)}(t)$ at the time moment ranging from $-T/2$ to $T/2$. Since $\Psi_{F/B}^{(l)}(t)$ is also a periodic function which has the period of T , $\psi_{F/B,n}^{(l)}$ can be also obtained through inverse Fourier transform:

$$\begin{aligned} \psi_{F,n}^{(l)} &= \frac{1}{T} \int_{-T/2}^{T/2} \Psi_F^{(l)}(t) e^{in\omega t} dt \\ &= \frac{1}{T} \int_{-T/2}^{T/2} \Phi_F^{(l)}(t) e^{in\omega t} dt \\ &= \frac{1}{T} \int_{-lT-T/2}^{-lT+T/2} \Phi_F^{(0)}(t) e^{in\omega t} dt, \quad (\text{A33}) \\ \psi_{B,n}^{(l)} &= \frac{1}{T} \int_{-T/2}^{T/2} \Psi_B^{(l)}(t) e^{in\omega t} dt \\ &= \frac{1}{T} \int_{-T/2}^{T/2} \Phi_B^{(l)}(t) e^{in\omega t} dt \\ &= \frac{1}{T} \int_{lT-T/2}^{lT+T/2} \Phi_B^{(0)}(t) e^{in\omega t} dt. \quad (\text{A34}) \end{aligned}$$

For the atomic displacements in the zeroth unit cell of SFLR and SBLR, its time evolution can be expressed as the sum of Fourier series as

$$\Phi_F^{(0)}(t) = \sum_m \sum_j \phi_{F,m,j}^{(0)} e^{-i\omega_{F,m,j} t}, \quad (\text{A35})$$

$$\Phi_B^{(0)}(t) = \sum_m \sum_j \phi_{B,m,j}^{(0)} e^{-i\omega_{B,m,j} t}, \quad (\text{A36})$$

where $\omega_{F,m,j}$ and $\omega_{B,m,j}$ are the excited frequencies of atomic vibrations ranging from $(m-1/2)\omega$ to $(m+1/2)\omega$ in SFLR and SBLR, respectively, and m is the positive integer varying from 1 to ∞ . The subscript j denotes the vibrational mode excited in corresponding regions. By selecting the appropriate m , $\omega_{F,m,j}$ and $\omega_{B,m,j}$ can take any values for frequency larger than $\omega/2$. Categorizing the excitation frequencies $\omega_{F,m,j}$ and $\omega_{B,m,j}$ in terms of m and j would facilitate the subsequent derivation. Substituting Eq. (A35) and Eq. (A36) into Eq. (A33) and Eq. (A34), we can obtain

$$\begin{aligned} \psi_{F,n}^{(l)} &= \frac{1}{T} \int_{-lT-T/2}^{-lT+T/2} \sum_m \sum_j \phi_{F,m,j}^{(0)} e^{-i(\omega_{F,m,j}-n\omega)t} dt \\ &= \sum_m \sum_j \frac{\sin(q_{F,m,n,j})}{q_{F,m,n,j}} \phi_{F,m,j}^{(0)} e^{2ilq_{F,m,n,j}}, \quad (\text{A37}) \end{aligned}$$

$$\begin{aligned} \psi_{B,n}^{(l)} &= \frac{1}{T} \int_{lT-T/2}^{lT+T/2} \sum_m \sum_j \phi_{B,m,j}^{(0)} e^{-i(\omega_{B,m,j}-n\omega)t} dt \\ &= \sum_m \sum_j \frac{\sin(q_{B,m,n,j})}{q_{B,m,n,j}} \phi_{B,m,j}^{(0)} e^{-2ilq_{B,m,n,j}}, \quad (\text{A38}) \end{aligned}$$

where $q_{F/B,m,n,j} = (\omega_{F/B,m,j} - n\omega)(T/2)$. Notice that only for $m = n$, we have $-\pi/2 \leq q_{F/B,m,n,j} < \pi/2$ ($q_{F/B,m,n,j}$ is the abbreviation of $q_{F/B,m,n,j}$) according to the defined range of $\omega_{F/B,m,j}$. For $m \neq n$, $q_{F/B,m,n,j}$ is out of the range from $-\pi/2$ to $\pi/2$, leading to the tiny values of $\sin(q_{F/B,m,n,j})/q_{F/B,m,n,j}$ in Eqs. (A37) and (A38). Thus, an approximation is made in the following derivation that the terms with $m \neq n$ are ignored in Eqs. (A37) and (A38), and then we can obtain

$$\psi_{F,n}^{(l)} = \sum_j \frac{\sin(q_{F,n,j})}{q_{F,n,j}} \phi_{F,n,j}^{(0)} e^{2ilq_{F,n,j}}, \quad (\text{A39})$$

$$\psi_{B,n}^{(l)} = \sum_j \frac{\sin(q_{B,n,j})}{q_{B,n,j}} \phi_{B,n,j}^{(0)} e^{-2ilq_{B,n,j}}. \quad (\text{A40})$$

On the other hand, if we consider a certain vibrational component of $\Psi_F^{(l)}(t)$, i.e., $\psi_{F,n}^{(l)} e^{-in\omega t}$, as the response to $\psi_{F,n}^{(0)} e^{-in\omega t}$ induced by the wave propagating in the moving FLR, and consider a certain vibrational component of $\Psi_B^{(l)}(t)$, i.e., $\psi_{B,n}^{(l)} e^{-in\omega t}$, as the response to $\psi_{B,n}^{(0)} e^{-in\omega t}$ induced by the wave propagating in the moving BLR, $\psi_{F,n}^{(l)}$ and $\psi_{B,n}^{(l)}$ can be expressed as [15,24,25]

$$\begin{aligned} \psi_{F,n}^{(l)} &= B_{F,n}^l \psi_{F,n}^{(0)} = U_{F,n} \Lambda_{F,n}^l U_{F,n}^{-1} \phi_{F,n}^{(0)} \\ &= \sum_j [U_{F,n}]_{:,j} [U_{F,n}^{-1}]_{j,:} \psi_{F,n}^{(0)} e^{il\kappa_{F,n,j} a_x}, \quad (\text{A41}) \end{aligned}$$

$$\begin{aligned} \psi_{B,n}^{(l)} &= B_{B,n}^l \psi_{B,n}^{(0)} = U_{B,n} \Lambda_{B,n}^l U_{B,n}^{-1} \phi_{B,n}^{(0)} \\ &= \sum_j [U_{B,n}]_{:,j} [U_{B,n}^{-1}]_{j,:} \psi_{B,n}^{(0)} e^{il\kappa_{B,n,j} a_x}, \quad (\text{A42}) \end{aligned}$$

where $B_{F,n}$ and $B_{B,n}$ are the Bloch matrices, denoting the changes in amplitude and phase as the wave propagates from one unit cell to another in FLR and BLR, which can be solved as $B_{F/B,n} = \tilde{g}_{F/B,n} H_{F/B,n}^{10}$. $U_{F/B,n}$ is the eigenmatrix with its columns consisting of the vibrational eigenstates, i.e., the phonon modes. $\Lambda_{F/B,n}$ is a diagonal matrix with its diagonal elements consisting of the vibrational eigenvalues as $\lambda_{F/B,n}^{(j)} \propto e^{il\kappa_{F/B,n,j} a_x}$ [15,24,25], where $\kappa_{F/B,n,j}$ is the corresponding wave vectors of phonon with mode j excited in FLR or BLR at $n\omega$. The subscripts “:, j ” and “ j , :” represent the j th column and j th row of the matrix, respectively, denoting the j th phonon mode. Equation (A41) and Eq. (A42) are derived based on the propagation approximation. This approximation assumes that the waves excited by $\psi_{F,n}^{(0)} e^{-in\omega t}$ and $\psi_{B,n}^{(0)} e^{-in\omega t}$ could propagate in the moving FLR and BLR with velocities identical to those of phonons excited in the SFLR and SBLR with the same excitation frequency. This approximation is valid because the moving velocity of FLR and BLR is rather small compared with the phonon group velocity. Thus, combining

Eqs. (A39) and (A40) and Eqs. (A41) and (A42), we can obtain the following relations:

$$\begin{aligned} & \sum_j \frac{\sin(q_{F,n,j})}{q_{F,n,j}} \phi_{F,n,j}^{(0)} e^{2ilq_{F,n,j}} \\ &= \sum_j [U_{F,n}]_{:,j} [U_{F,n}^{-1}]_{j,:} \psi_{F,n}^{(0)} e^{il\kappa_{F,n,j}a_x}, \end{aligned} \quad (\text{A43})$$

$$\begin{aligned} & \sum_j \frac{\sin(q_{B,n,j})}{q_{B,n,j}} \phi_{B,n,j}^{(0)} e^{-2ilq_{B,n,j}} \\ &= \sum_j [U_{B,n}]_{:,j} [U_{B,n}^{-1}]_{j,:} \psi_{B,n}^{(0)} e^{il\kappa_{B,n,j}a_x}. \end{aligned} \quad (\text{A44})$$

Notice that Eqs. (A43) and (A44) hold true regardless of the value chosen for the parameter l . Given the relations of $q_{F,n,j} = \kappa_{F,n,j}a_x/2$ and $-q_{B,n,j} = \kappa_{B,n,j}a_x/2$, we can obtain $\omega_{F,n,j} = n\omega + \kappa_{F,n,j}v_0$ and $\omega_{B,n,j} = n\omega - \kappa_{B,n,j}v_0$ in SFLR and SBLR, respectively, according to $q_{F/B,n,j} = (\omega_{F/B,n,j} - n\omega)(T/2)$. Actually, the solved $\omega_{F,n,j}$ and $\omega_{B,n,j}$ are the frequencies of friction-excited phonons in SFLR and SBLR. Notice that $\kappa_{F/B,n,j}$ always satisfies the following relations as $-\pi \leq \kappa_{F/B,n,j}a_x < \pi$ in the first Brillouin zone. Thus, $\omega_{F/B,n,j}$ always ranges from $(n-1/2)\omega$ to $(n+1/2)\omega$ in SFLR and SBLR according to $\omega_{F/B,n,j} = n\omega \pm \kappa_{F/B,n,j}v_0$, whose definition is self-consistent in Eqs. (A35) and (A36).

After simplifications, $\phi_{F,n,j}^{(0)}$ and $\phi_{B,n,j}^{(0)}$ in Eq. (A43) and Eq. (A44), which represent the excited atomic vibrations at $\omega_{F,n,j}$ and $\omega_{B,n,j}$, respectively, can be expressed as follows:

$$\phi_{F,n,j}^{(0)} = [U_{F,n}]_{:,j} [U_{F,n}^{-1}]_{j,:} \psi_{F,n}^{(0)} \frac{q_{F,n,j}}{\sin(q_{F,n,j})}, \quad (\text{A45})$$

$$\phi_{B,n,j}^{(0)} = [U_{B,n}]_{:,j} [U_{B,n}^{-1}]_{j,:} \psi_{B,n}^{(0)} \frac{q_{B,n,j}}{\sin(q_{B,n,j})}. \quad (\text{A46})$$

Here, it is sufficient to solve the atomic vibration displacements, denoted as $\phi_{F,n,j}^{(0)}$ for the zeroth unit cells in the SFLR and $\phi_{B,n,j}^{(0)}$ for the zeroth unit cell in the SBLR. This stems from the fact that the vibrational characteristics of atoms in subsequent unit cells, namely the 1st, 2nd, and p th unit cells within SFLR or SBLR, are consistent with those in the zeroth unit cells. The only distinction arises in the phase difference, which does not affect the overall analysis. Then, the friction-generated heat flux, i.e., the dissipated energy carried by phonons excited in SFLR and SBLR, respectively, can be calculated as

$$Q_{F,n,j} = \frac{1}{2a_x} \omega_{F,n,j}^2 (U_{F,n}^{-1} \phi_{F,n,j}^{(0)})^\dagger V_{F,n,j} U_{F,n}^{-1} \phi_{F,n,j}^{(0)}, \quad (\text{A47})$$

$$Q_{B,n,j} = \frac{1}{2a_x} \omega_{B,n,j}^2 (U_{B,n}^{-1} \phi_{B,n,j}^{(0)})^\dagger V_{B,n,j} U_{B,n}^{-1} \phi_{B,n,j}^{(0)}, \quad (\text{A48})$$

where $U_{F/B,n,j}$ and $V_{F/B,n,j}$ represent the eigenmatrix and diagonal velocity matrix at $\omega_{F/B,n,j}$, respectively. $V_{F,n,j}$ and $V_{B,n,j}$ can be further expressed as follows [15,24,25]:

$$V_{F,n,j} = \frac{a_x}{2\omega_{F,n,j}} U_{F,n,j}^\dagger \Gamma_{F,n,j} U_{F,n,j}, \quad (\text{A49})$$

$$V_{B,n,j} = \frac{a_x}{2\omega_{B,n,j}} U_{B,n,j}^\dagger \Gamma_{B,n,j} U_{B,n,j}, \quad (\text{A50})$$

where $\Gamma_{F/B,n,j} = i(\Sigma_{F/B,n,j}^{00} - \Sigma_{F/B,n,j}^{0\ddagger})$, with $\Sigma_{F/B,n,j}^{00}$ representing the self-energy matrix for uncontacted FLR or BLR at $\omega_{F/B,n,j}$. According to Eqs. (A47) and (A48), the friction force per unit area can be calculated as the total dissipated heat flux divided by the average velocity of the slider and the contact area (S) as follows:

$$F = \frac{\sum_n \sum_j (Q_{F,n,j} + Q_{B,n,j})}{Sv_0}. \quad (\text{A51})$$

Moreover, the number density of excited phonons in FLR and BLR can be calculated as follows:

$$N_{F,n,j} = \frac{\omega_{F,n,j} (U_{F,n}^{-1} \phi_{F,n,j}^{(0)})^\dagger U_{F,n}^{-1} \phi_{F,n,j}^{(0)}}{2\hbar\Omega}, \quad (\text{A52})$$

$$N_{B,n,j} = \frac{\omega_{B,n,j} (U_{B,n}^{-1} \phi_{B,n,j}^{(0)})^\dagger U_{B,n}^{-1} \phi_{B,n,j}^{(0)}}{2\hbar\Omega}, \quad (\text{A53})$$

where Ω is the volume of the unit cell in the two lead regions.

APPENDIX B: PROOFS OF PHONON EXCITATION RULE UNDER THE DOPPLER EFFECT

Notice that Eqs. (A41) and (A42) are derived based on the propagation approximation, which can dramatically simplify the calculations but introduce the deviation. If we do not apply the propagation approximation, $\psi_{F,n}^{(l)}$ and $\psi_{B,n}^{(l)}$ can be expressed similar to Eq. (A37) and Eq. (A38) as

$$\begin{aligned} \psi_{F,n}^{(l)} &= \frac{1}{T} \int_{-\frac{T}{2}}^{\frac{T}{2}} \sum_m \sum_j \phi_{F,m,j}^{(l)} e^{-i(n\omega - \omega_{F,m,j})t} dt \\ &= \sum_m \sum_j \frac{\sin(q_{F,m,n,j})}{q_{F,m,n,j}} B_{F,m,j}^l \phi_{F,m,j}^{(0)}, \end{aligned} \quad (\text{B1})$$

$$\begin{aligned} \psi_{B,n}^{(l)} &= \frac{1}{T} \int_{-\frac{T}{2}}^{\frac{T}{2}} \sum_m \sum_j \phi_{B,m,j}^{(l)} e^{-i(n\omega - \omega_{B,m,j})t} dt \\ &= \sum_m \sum_j \frac{\sin(q_{B,m,n,j})}{q_{B,m,n,j}} B_{B,m,j}^l \phi_{B,m,j}^{(0)}, \end{aligned} \quad (\text{B2})$$

where $B_{F,m,j}$ and $B_{B,m,j}$ are the Bloch matrices with frequencies of $\omega_{F,m,j}$ and $\omega_{B,m,j}$, respectively. Notice that $B_{F/B,m,j}^l \phi_{F/B,m,j}^{(0)} = e^{il\tilde{\kappa}_{F/B,m,j}a_x} \phi_{F/B,m,j}^{(0)}$ holds true because $\phi_{F/B,m,j}^{(0)}$ defined in Eqs. (A35) and (A36) is already a vibrational eigenstate of $B_{F/B,m,j}$ with eigenvalue of $e^{i\tilde{\kappa}_{F/B,m,j}a_x}$. Here, $\tilde{\kappa}_{F/B,m,j}$ is different from $\kappa_{F/B,m,j}$, which represents the corresponding wave vectors of phonon with mode j excited at $\omega_{F/B,m,j}$ in SFLR or SBLR, while $\kappa_{F/B,m,j}$ is the corresponding wave vectors of phonon with mode j excited at $m\omega$ in FLR or BLR. Combining Eqs. (A37) and (A38) and Eqs. (B1) and (B2), we can obtain the following relations as

$$\begin{aligned} & \sum_m \sum_j \frac{\sin(q_{F,m,n,j})}{q_{F,m,n,j}} \phi_{F,m,j}^{(0)} e^{il\tilde{\kappa}_{F,m,j}a_x} \\ &= \sum_m \sum_j \frac{\sin(q_{F,m,n,j})}{q_{F,m,n,j}} \phi_{F,m,j}^{(0)} e^{2ilq_{F,m,n,j}}, \end{aligned} \quad (\text{B3})$$

$$\begin{aligned} & \sum_m \sum_j \frac{\sin(q_{B,m,n,j})}{q_{B,m,n,j}} \phi_{B,m,j}^{(0)} e^{il\tilde{\kappa}_{B,m,j}a_x} \\ &= \sum_m \sum_j \frac{\sin(q_{B,m,n,j})}{q_{B,m,n,j}} \phi_{B,m,j}^{(0)} e^{-2ilq_{B,m,n,j}}. \end{aligned} \quad (\text{B4})$$

Also, Eqs. (B3) and (B4) hold true regardless of the value chosen for the parameter l , implying the relations of $q_{F,m,n,j} + h_F\pi = \tilde{\kappa}_{F,m,j}a_x/2$ and $-q_{B,m,n,j} + h_B\pi = \tilde{\kappa}_{B,m,j}a_x/2$, where h_F and h_B are the arbitrary integers. Notice that $q_{F/B,m,n,j}$ varies with different n , but $\tilde{\kappa}_{F/B,m,j}$ does not. To make the above relations independent of n , we can make $h_F = (n-m)\pi$ and $h_B = (m-n)\pi$, and obtain $q_{F,m,n,j} + h_F\pi = q_{F,m,j}$ and $q_{B,m,n,j} - h_B\pi = q_{B,m,j}$. Finally, according to the above relations, we can further obtain the relations of $\omega_{F,m,j} = m\omega + \tilde{\kappa}_{F,m,j}v_0$ and $\omega_{B,m,j} = m\omega - \tilde{\kappa}_{B,m,j}v_0$ in SFLR and SBRL, respectively, according to $q_{F/B,m,j} = (\omega_{F/B,m,j} - m\omega)T/2$. The relations of $\omega_{F,m,j} = m\omega + \tilde{\kappa}_{F,m,j}v_0$ and $\omega_{B,m,j} = m\omega - \tilde{\kappa}_{B,m,j}v_0$ prove the phonon excitation rule that the friction-excited phonon frequency can be determined by the intersections between the kinematic lines and dispersion relation curves as shown in Fig. 3(b).

Notice that the predicted phonon excitation frequency of $\omega_{F/B,n,j} = n\omega \pm \kappa_{F/B,n,j}v_0$ derived from Eqs. (A43) and (A44) shows a slight deviation from the prediction based on the phonon excitation rule as $\omega_{F/B,n,j} = n\omega \pm \tilde{\kappa}_{F/B,n,j}v_0$, as caused by the propagation approximation. The difference lies in that $\kappa_{F/B,n,j}$ is determined by the points where the static lines intersect the dispersion relation curves, while $\tilde{\kappa}_{F/B,n,j}$ is determined by the points where the kinematic lines intersect the dispersion relation curves. The values of $\omega_{F/B,n,j}$ determined by $\kappa_{F/B,n,j}$ and $\tilde{\kappa}_{F/B,n,j}$, respectively converge at a low

sliding velocity, indicating that this deviation is insignificant at low sliding velocity.

APPENDIX C: DETAILS OF MOLECULAR DYNAMICS SIMULATIONS

To verify the predicted frequency shifts from the PD model, the molecular dynamics simulations are conducted using LAMMPS [19]. The friction system is composed of a graphene flake sliding over another graphene substrate as shown in Fig. 4(a). The top rectangle graphene flake works as a slider with area of $2.5 \times 2.6 \text{ nm}^2$. The graphene substrate is set with area of $49.8 \times 2.6 \text{ nm}^2$, while two thermostats are set with area of $11.2 \times 2.6 \text{ nm}^2$ at both ends of substrate. Each carbon atom on the slider is connected with three virtual supports through three springs along the x -, y -, and z directions, respectively. All springs are set with the same stiffness of 0.1 N/m , whose value is the same as that in the PD model. The x -axis virtual support drags the x -axis springs with a constant velocity of 100 m/s to drive the slider sliding over the substrate, while the y - and z -axis supports restrain the slider movement along the y - and z directions through the corresponding springs attached to each atom on the slider. Periodic boundary conditions are only applied along the y direction. The normal load on each slider atom is set as 0.1 nN , while the intralayer atomic interactions and the interlayer atomic interactions of graphene are set the same as those parameters in the PD model. In the MD model, the thermostats are set as heat sinks to absorb the friction-generated heat flux, which plays the same role as the lead region in the PD model. Besides, the fixed wall must be set in the MD atomic model to avoid the distortion of the substrate in the MD simulations. The video visualizations of MD simulations with visual friction-excited lattice waves can be found in the Supplemental Material [26].

-
- [1] C. Doppler, *Ueber das Farbige Licht der Doppelsterne und Einiger Anderer Gestirne des Himmels: Versuch Einer das Bradley'sche Aberrations-Theorem als Integrirenden Theil in Sich Schliessenden Allgemeineren Theorie* (K. Böhm Ges. Wiss., Prag, Österreich-Ungarn, 1903).
- [2] F. Guo, Y. Yang, F. Ma, Y. Zhu, H. Liu, and X. Zhang, Instantaneous velocity determination and positioning using Doppler shift from a LEO constellation, *Satell. Navig.* **4**, 9 (2023).
- [3] D. H. Atkinson, J. B. Pollack, and A. Seiff, Galileo Doppler measurements of the deep zonal winds at Jupiter, *Science* **272**, 842 (1996).
- [4] D. L. Franklin, W. Schlegel, and R. F. Rushmer, Blood flow measured by Doppler frequency shift of back-scattered ultrasound, *Science* **134**, 564 (1961).
- [5] J. Zhang, K. Zhang, R. Grenfell, and R. Deakin, Short Note: On the relativistic Doppler effect for precise velocity determination using GPS, *J. Geodesy* **80**, 104 (2006).
- [6] W. D. Phillips, J. V. Prodan, and H. J. Metcalf, Laser cooling and electromagnetic trapping of neutral atoms, *J. Opt. Soc. Am. B* **2**, 1751 (1985).
- [7] N. B. Vilas, C. Hallas, L. Anderegg, P. Robichaud, A. Winnicki, D. Mitra, and J. M. Doyle, Magneto-optical trapping and sub-Doppler cooling of a polyatomic molecule, *Nature (London)* **606**, 70 (2022).
- [8] L. Prandtl, A conceptual model to the kinetic theory of solid bodies, *Z. Angew. Math. Mech* **8**, 85 (1928).
- [9] G. A. Tomlinson, CVI. A molecular theory of friction, *Philos. Mag. (1798-1977)* **7**, 905 (1929).
- [10] J. H. Dieterich, Modeling of rock friction: 1. Experimental results and constitutive equations, *J. Geophys. Res: Solid Earth* **84**, 2161 (1979).
- [11] A. Ruina, Slip instability and state variable friction laws, *J. Geophys. Res.: Solid Earth* **88**, 10359 (1983).
- [12] S. N. Medyanik, W. K. Liu, I.-H. Sung, and R. W. Carpick, Predictions and observations of multiple slip modes in atomic-scale friction, *Phys. Rev. Lett.* **97**, 136106 (2006).
- [13] A. Socoliuc, R. Bennewitz, E. Gnecco, and E. Meyer, Transition from stick-slip to continuous sliding in atomic friction: Entering a new regime of ultralow friction, *Phys. Rev. Lett.* **92**, 134301 (2004).
- [14] M. M. Scuderi, C. Collettini, and C. Marone, Frictional stability and earthquake triggering during fluid pressure stimulation of an experimental fault, *Earth Planet. Sci. Lett.* **477**, 84 (2017).

- [15] Y. Tao, Z. Wei, Y. Dong, Z. Duan, Y. Kan, Y. Zhang, and Y. Chen, Phononic dynamics in sliding friction, *Phys. Rev. B* **108**, 214313 (2023).
- [16] L. Lindsay and D. A. Broido, Optimized Tersoff and Brenner empirical potential parameters for lattice dynamics and phonon thermal transport in carbon nanotubes and graphene, *Phys. Rev. B* **81**, 205441 (2010).
- [17] L. A. Girifalco, M. Hodak, and R. S. Lee, Carbon nanotubes, buckyballs, ropes, and a universal graphitic potential, *Phys. Rev. B* **62**, 13104 (2000).
- [18] Z. Duan, Z. Wei, S. Huang, Y. Wang, C. Sun, Y. Tao, Y. Dong, J. Yang, Y. Zhang, Y. Kan *et al.*, Resonance in atomic-scale sliding friction, *Nano Lett.* **21**, 4615 (2021).
- [19] S. Plimpton, Fast parallel algorithms for short-range molecular dynamics, *J. Comput. Phys.* **117**, 1 (1995).
- [20] S. Sadasivam, Y. Che, Z. Huang, L. Chen, S. Kumar, and T. S. Fisher, The atomistic Green's function method for interfacial phonon transport, *Annu. Rev. Heat Transfer* **17**, 89 (2014).
- [21] S. Datta, *Quantum Transport: Atom to Transistor* (Cambridge University Press, Cambridge, UK, 2005).
- [22] J.-S. Wang, J. Wang, and J. T. Lü, Quantum thermal transport in nanostructures, *Eur. Phys. J. B* **62**, 381 (2008).
- [23] W. Zhang, T. S. Fisher, and N. Mingo, Simulation of interfacial phonon transport in Si-Ge heterostructures using an atomistic Green's function method, *J. Heat Transfer* **129**, 483 (2006).
- [24] Z.-Y. Ong and G. Zhang, Efficient approach for modeling phonon transmission probability in nanoscale interfacial thermal transport, *Phys. Rev. B* **91**, 174302 (2015).
- [25] B. Latour, N. Shulumba, and A. J. Minnich, Ab initio study of mode-resolved phonon transmission at Si/Ge interfaces using atomistic Green's functions, *Phys. Rev. B* **96**, 104310 (2017).
- [26] See Supplemental Material at <http://link.aps.org/supplemental/10.1103/PhysRevB.109.205410> for the video visualizations of molecular dynamics simulations. The supplemental videos clearly illustrate the friction-excited lattice waves formed by atomic z -displacement (unit: Å), i.e., the ZA-mode phonons in the quantized forms. It is obvious that the wavelengths of the lattice waves in front and rear of the slider are compressed and lengthened respectively, a phenomenon consistent with the phononic Doppler effect.